Initial observations of lunar impact melts and ejecta flows with the Mini-RF radar

Lynn M. Carter,[1] Catherine D. Neish,[2] D. B. J. Bussey,[2] Paul D. Spudis,[3] G. Wesley Patterson,[2] Joshua T. Cahill,[2] and R. Keith Raney[2]

Received 29 July 2011; revised 1 December 2011; accepted 3 December 2011; published 21 February 2012.

[1] The Mini-RF radar on the Lunar Reconnaissance Orbiter spacecraft has revealed a great variety of crater ejecta flow and impact melt deposits, some of which were not observed in prior radar imaging. The craters Tycho and Glushko have long melt flows that exhibit variations in radar backscatter and circular polarization ratio along the flow. Comparison with optical imaging reveals that these changes are caused by features commonly seen in terrestrial lava flows, such as rafted plates, pressure ridges, and ponding. Small (<20 km) sized craters also show a large variety of deposits, including melt flows and ponds. Two craters have flow features that may be ejecta flows caused by entrained debris flowing across the surface rather than by melted rock. The circular polarization ratios (CPRs) of the impact melt flows are typically very high; even ponded areas have CPR values between 0.7 and 1.0. This high CPR suggests that deposits that appear smooth in optical imagery may be rough at centimeter- and decimeter- scales. In some places, ponds and flows are visible with no easily discernable source crater. These melt deposits may have come from oblique impacts that are capable of ejecting melted material farther downrange. They may also be associated with older, nearby craters that no longer have a radar-bright proximal ejecta blanket. The observed morphology of the lunar crater flows has implications for similar features observed on Venus. In particular, changes in backscatter along many of the ejecta flows are probably caused by features typical of lava flows.

Citation: Carter, L. M., C. D. Neish, D. B. J. Bussey, P. D. Spudis, G. W. Patterson, J. T. Cahill, and R. K. Raney (2012), Initial observations of lunar impact melts and ejecta flows with the Mini-RF radar, *J. Geophys. Res.*, *117*, E00H09, doi:10.1029/2011JE003911.

1. Introduction

[2] The impact process generates substantial melted material that is deposited in and around the crater. Early observations of the Moon revealed melt features associated with fresh impact craters; these features included thin veneers, ponds, and flows [*Shoemaker et al.*, 1968; *Guest*, 1973; *Howard and Wilshire*, 1975; *Hawke and Head*, 1977]. *Hawke and Head* [1977] found that the types and distribution of melt associated with impacts varies with crater size; craters with diameters less than 10 km were observed to have mostly veneers and small ponds on and outside the rims, while larger 20–50 km diameter craters are more likely to have significant melt flows. Ponds and melt flows can be found up to two crater radii from the rim of lunar craters, and the largest craters (above 50 km diameter) were observed to have ponds, but no flows [*Hawke and Head*, 1977].

[3] Magellan radar images of Venus also revealed long impact crater ejecta flows with complex radar backscatter variations that extend up to 14 crater radii from the rims [*Phillips et al.*, 1991; *Chadwick and Schaber*, 1993; *Asimow and Wood*, 1992]. The transitions between radar bright and radar dark backscatter within a given flow have been attributed to various types of surface roughness changes, including differences in entrained clast abundance along the flow [*Chadwick and Schaber*, 1993], deposition of rough, blocky material caused by topographic obstruction of a transient impact-induced hot vapor cloud [*Schultz*, 1992], or changes in lava-like flow features that form in flowing impact melt [*Johnson and Baker*, 1994].

[4] There are also multiple models for ejecta flow formation, which fall into two major categories. The first group of models suggests that the flows are caused by hot, turbulent density currents similar to pyroclastic flows that entrain melt, vapor and debris [*Shoemaker et al.*, 1968; *Phillips et al.*, 1991; *Schultz*, 1992]. This flow emplacement mechanism is sometimes suggested to be an early stage process, particularly because proximal crater ejecta blanket materials often appear to overlie flow features on Venus [*Asimow and*

[1]Planetary Geodynamics Laboratory, NASA Goddard Space Flight Center, Greenbelt, Maryland, USA.
[2]Johns Hopkins University Applied Physics Laboratory, Laurel, Maryland, USA.
[3]Lunar and Planetary Institute, Houston, Texas, USA.

Copyright 2012 by the American Geophysical Union.
0148-0227/12/2011JE003911

Wood, 1992]. In this case, crater ejecta may have flow-like boundaries that are produced primarily by deposition of solid debris rather than by flowing melted rock.

[5] A second hypothesis suggests that, subsequent to ejecta emplacement, melted rock undergoes late-stage segregation and then travels over the surface like a lava flow [*Shoemaker et al.*, 1968; *Phillips et al.*, 1991; *Asimow and Wood*, 1992; *Johnson and Baker*, 1994]. In this case, the flow boundaries are created by the impact melt, which likely entrains both country rock and ejecta clasts as it flows over and around the previously emplaced ejecta. For the Venus craters, it is possible that both processes (debris-rich flows and flowing impact melt) can occur and this leads to the variety of different flow morphologies seen in radar images. The prevalence and length of the ejecta flows on Venus are likely due to a combination of factors, including the high surface temperatures, high mean impact velocities, and high atmospheric pressure [*Phillips et al.*, 1991; *Asimow and Wood*, 1992].

[6] There are multiple physical parameters that influence the emplacement of melted rock during and after impacts. The angle of impact controls the direction of ejected material and can lead to increased deposition of melt downrange and to the sides of the impact site [*Schultz*, 1996; *Pierazzo and Melosh*, 2000]. Impact angle is often cited as one of the primary contributors to large amounts of melt deposition outside the crater [*Hawke and Head*, 1977; *Phillips et al.*, 1991]. Melt flows will contain some component of unmelted country rock clasts produced by the impact event, of which increasing amounts will increase the viscosity of the flow. Topographic gradients can allow melt to escape from the crater walls, speed or slow the flow as it travels across the surface, or trap melt material in topographic lows to form ponds [*Hawke and Head*, 1977; *Johnson and Baker*, 1994]. Recent images from the Lunar Reconnaissance Orbiter Camera (LROC) Narrow Angle Camera (NAC) have shown a complex evolution of melt flows, including multiple-stage melt injection, flow inflation, erosion of crater walls and uphill movement of melt [*Bray et al.*, 2010]. These processes suggest that the formation of melt flow features may vary extensively depending on the impact conditions, and may have relatively long cooling times [*Bray et al.*, 2010].

[7] Radar observations of the lunar melt flows can provide additional information beyond what can be learned with optical imaging. Radar is sensitive to roughness on the scale of the radar wavelength, and at S-band wavelengths (12.6 cm), it can be used to assess surface and subsurface roughness of the centimeter to decimeter scale. This is somewhat smaller than what is directly visible in high-resolution imaging, including the LROC NAC, which has a 50 cm/pixel resolution [*Robinson et al.*, 2010]. For typical lunar regolith dielectric properties [*Carrier et al.*, 1991], the 12.6 cm wavelength Mini-RF radar wave can penetrate up to ~1 m below the surface. This allows detection of buried impact melt and associated flow structures that have been smoothed over by regolith deposition and maturation and are consequently no longer visible in optical images [e.g., *Campbell et al.*, 2010].

[8] Prior radar observations of lunar impact craters using Arecibo Observatory S-band (12.6 cm wavelength) radar system and the Green Bank Telescope have revealed rough, radar bright flows that can extend greater than two crater radii from the rim [*Campbell et al.*, 2010]. Some of these flows had not been previously identified in imaging data (e.g., Aristillus) [*Campbell et al.*, 2010]. The melt flows have very high values of the radar circular polarization ratio, which suggests that the flow surfaces have roughness characteristics greater than terrestrial a'a lavas [*Campbell et al.*, 2010]. The Mini-RF radar on LRO can likewise be used to assess melt flow roughness, to determine whether there is structure internal to the flow, and to map flow boundaries, all of which can lead to a better understanding of how impact melt and debris flows are emplaced. Mini-RF has a somewhat higher resolution (15 × 30 m/pixel) than the highest resolution ground-based radar data (20–30 m/pixel) [*Raney et al.*, 2011; *Campbell et al.*, 2010]. Mini-RF can also image the lunar farside and the lunar poles to search for examples of impact melts not previously observed by radar.

2. Mini-RF Polarimetric Data

[9] The Mini-RF instrument on the LRO has acquired S-band (12.6 cm wavelength) radar imagery of many impact craters at a resolution of 15 × 30 m [*Raney et al.*, 2011]. The radar transmits a circular-polarized wave and measures two orthogonal received polarizations (horizontal, H and vertical, V). These data can be used to generate images for each element of the Stokes vector [*Jackson*, 1999; *Green*, 1968]:

$$S = \begin{bmatrix} S_1 \\ S_2 \\ S_3 \\ S_4 \end{bmatrix} = \begin{bmatrix} \left\langle |E_H|^2 \right\rangle + \left\langle |E_V|^2 \right\rangle \\ \left\langle |E_H|^2 \right\rangle - \left\langle |E_V|^2 \right\rangle \\ 2\mathrm{Re}\left\langle E_H E_V^* \right\rangle \\ -2\mathrm{Im}\left\langle E_H E_V^* \right\rangle \end{bmatrix} \quad (1)$$

The first Stokes parameter image (S_1) is a measure of the total average power of the echo. The S_2 and S_3 Stokes parameter images measure the linearly polarized power, and the S_4 Stokes parameter image provides information on the magnitude of the circularly polarized power and whether it is right or left circular-polarized. These four polarization images are a primary data product of Mini-RF, and are mapped to the lunar coordinate grid with a resolution of 15 m/pixel. The center-swath incidence angle for flat surfaces varies from ~48–55°. Changes in surface topography lead to a large range of incidence angles in many images, particularly images in highland terrains.

[10] The circular polarization ratio (CPR) can be used as an indicator of surface roughness. The CPR, which is the ratio of the same-sense circular polarization as was transmitted to the opposite-sense circular polarization as was transmitted, can be calculated from [*Stacy*, 1993]:

$$CPR = \frac{S_1 - S_4}{S_1 + S_4} \quad (2)$$

Surfaces that are very smooth at wavelength scales will lead to low CPR values (<0.4), while scattering from surfaces that are rough at the wavelength scale, and have double-bounce geometries, lead to moderate to high (0.4–1.0) CPR values. A double-bounce geometry occurs when the radar wave reflects from two surfaces before returning to the receiver, thereby causing the received circular polarization state to be the same as that transmitted. Extremely rugged

terrain can sometimes produce circular polarization ratios greater than one [e.g., *Campbell and Campbell*, 1992; *Campbell*, 2009]. These high CPR values cannot be caused by Bragg scattering from wavelength scale roughness [e.g., *Ulaby et al.*, 1986] and require that a significant amount of the backscatter come from double-bounce geometries. For terrestrial analog surfaces, CPR values near or above one correspond to surfaces that have a rugged appearance and are rough at centimeter to meter, and sometimes decimeter, scales [e.g., *Campbell and Campbell*, 1992].

[11] The circular polarization ratio also changes with incidence angle (lunar examples can be found in the works of *Campbell et al.* [2010] and *Carter et al.* [2011, 2009]), because at low (nadir) incidence angles, the backscatter is dominated by mirror-like quasi-specular scattering. Therefore, we compare CPR values for surfaces that were observed at similar incidence angles. For this paper, the CPR images were derived by averaging the S1 and S4 images to a resolution of 60 m/pixel and then forming the CPR. This extra averaging reduces the radar speckle noise and therefore improves the visibility of some polarization features.

[12] The Mini-RF data sometimes have a gradient in the circular polarization ratio across the range (or horizontal) dimension of the image and the circular polarization values given in this paper have uncertainties related to this issue. Gradients as large as 0.3 have been measured for a few images, but gradients between 0.1 and 0.2 are more common. These values exceed the change in CPR that could be caused by the few degree incidence angle change across the swath width (range dimension). Prior measurements of the lunar surface at the Mini-RF wavelength (S-band) show that CPR changes by only a few tenths as the incidence angle changes by ~5° [*Campbell et al.*, 2010; *Carter et al.*, 2009]. For two craters discussed in this paper (Glushko, Aristillus), Mini-RF data were acquired at a similar incidence angle to published ground-based radar data and can be directly compared. In these cases, the CPR values are within 0.05 of those reported by *Campbell et al.* [2010], which suggests that the CPR values measured by Mini-RF are consistent with prior data.

[13] However, for lunar farside craters, there is no alternative data source to check the calibration. In an attempt to mitigate these issues, we have not used CPR measurements in cases where the gradient is particularly bad (e.g., more than +0.1 across the image). Most of the images used in this paper have a CPR gradient less than ~0.05. Because of the general match to ground-based data for the nearside cases, for the low- to moderate-gradient cases used here, we estimate that the systematic errors are no more than ±0.1. Below, we focus on comparing CPR values that are very high (greater than 1), high (0.7–1.0) and moderate (0.6–0.7), to avoid the need for precise CPR numbers. Additional calibration is currently ongoing to improve the quantitative polarimetry from Mini-RF.

3. Surface Properties of Melt Flows

[14] Mini-RF has mapped ~66% of the lunar surface at mean incidence angles (on flat terrain) between ~48°–54°, and has imaged many impact craters with ejecta flows and melt ponds. Below, we discuss the surface properties of some of these flow features for craters with different size ranges. The size divisions were chosen to roughly correspond to those used by *Hawke and Head* [1977], who found that the importance of melt flows relative to ponds and veneers varied partially based on impact crater size. The craters discussed here were chosen on the basis of a survey of initial Mini-RF data and are not a statistical sample. In particular, larger melt flows are easier to detect and it is possible that a systematic search of the data will reveal additional small and medium-sized craters with impact melt ponds and ejecta flows.

3.1. Large (50+ km Diameter) Impact Craters

[15] Impact flows associated with large (>50 km diameter) impact craters display a wide range of morphologies, including ponds and large flows. Melt flows of some craters within this size range can display significant variation in radar backscatter along the flow, and can look similar to radar images of impact crater flows on Venus [*Phillips et al.*, 1991; *Chadwick and Schaber*, 1993]. The 85 km diameter crater Tycho (43.3°S, 248.8°E) is one example [*Shoemaker et al.*, 1968]. Although Tycho is visible in Earth-based radar images, the thin flows are hard to detect in lower resolution Earth-based radar images.

[16] Mini-RF data of flows east of Tycho reveal both dark and bright sections of the melt flow that correspond to smooth and rough surfaces as seen in optical imagery (Figures 1 and 2). The bright areas of the flows typically have high CPR values (1.0–1.2). Radar dark parts of the flow can be difficult to distinguish from the surroundings, particularly since the mountainous terrain leads to a varying radar viewing geometry. However, even the radar-dark portions of the flow have fairly high CPR values, often in the range of 0.8 to 0.9. The lowest CPR values measured for very small parts of the smoothest melt ponds, away from any fresh impact craters or the rough edges of the ponds, are between 0.6 and 0.7. These values are still higher than what is measured for the non-melt flat surfaces in the area (CPR~0.55), and is higher than CPR values measured for most terrestrial a'a flows [*Campbell and Campbell*, 1992].

[17] High-resolution LROC NAC images of the upper stages of the flows (Figures 2a and 2b) show the differences in surface texture between smooth ponded melt material and rough flows. The high-CPR areas correspond to a rugged surface that looks similar to upturned platey pahoehoe or a'a flows (Figure 2a). The highest CPR values in this area of the flow are above 1.0, but are obscured by shadow in the LROC image. The CPR values in the non-shadowed rough regions of the LROC image are between 0.9 and 1.0, which is perhaps not surprising given the rugged surface. Nearby smooth areas have small craters, cooling fractures, and large angular blocks. These regions have CPR values of 0.7–0.8, which are still higher than the values measured for most terrestrial lava flows [*Campbell and Campbell*, 1992], despite a fairly smooth appearance.

[18] There are a couple of possible explanations for the high CPR values in areas that appear smooth in optical images; either the radar pixels nearly always incorporate enough rough features such as craters, fractures, or blocky regolith to create a high CPR, or the flow surface is very rough at the centimeter scale, possibly due to entrained clasts or to a rugged textured surface that is partially obscured by a coating of regolith. Fractured ponded lava and pahoehoe flows on Earth have CPR values that are lower than a'a lava [*Campbell and Campbell*, 1992], so an additional roughness

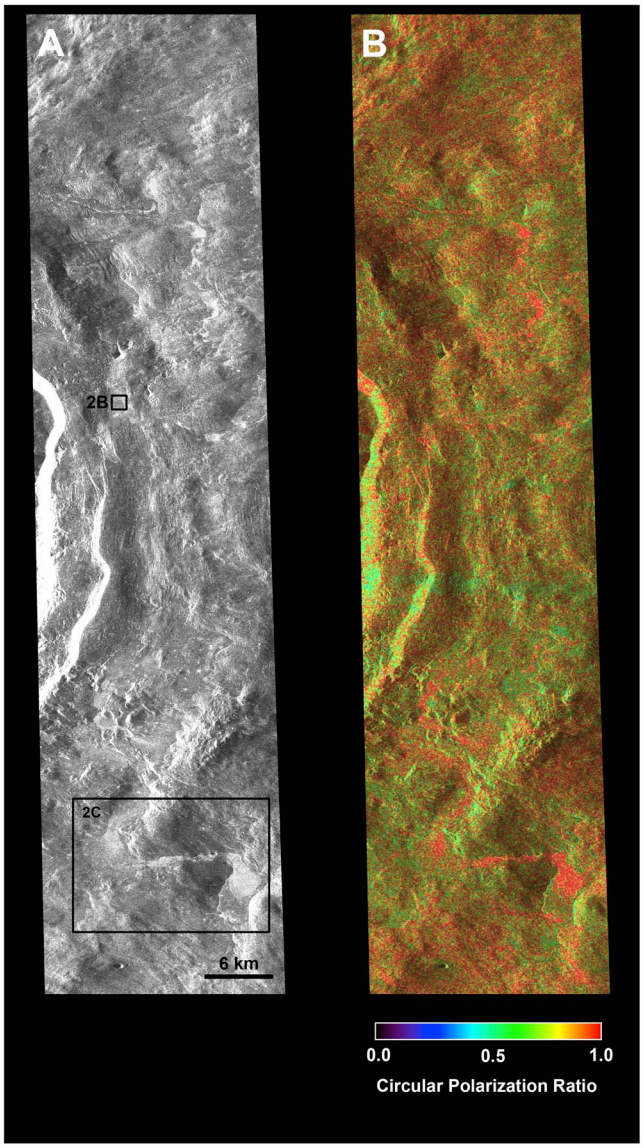

Figure 1. Mini-RF images of impact melt deposits to the east of Tycho. (a) A total power radar backscatter image. Radar illumination is from the left. (b) A CPR image stretched to a color scale and overlaid on the total power image. The Tycho ejecta deposits have very high CPR values, but the values are particularly large in radar-bright areas that correspond to very rugged impact melt flows. The positions of Figure 2b and 2c are marked on Figure 1a.

component beyond cooling cracks is likely present. The fact that even very small smooth areas of the melt flow have CPRs that are slightly above the average CPR value in the Tycho extended ejecta blanket suggests that there is a component of centimeter scale surface or near-surface roughness not apparent in current imagery.

[19] The Surveyor 7 spacecraft landed near the rim of Tycho and obtained surface photographs that reveal a complex near-rim geology. The area near the landing site has multiple types of flow-like features that have been attributed to movement of hot gas, debris and melt [*Shoemaker et al.*, 1968]. These flows do not have lava-like surface flow features like those seen in the eastern impact melt flows (Figure 2), but the surfaces of the Surveyor 7 flows are still very rough and exhibit varying degrees of cratering, likely from self-secondary impacts [*Shoemaker et al.*, 1968]. There are also many fields of angular blocks that are probably fall-back ejecta that was deposited during the later stages of the impact process [*Shoemaker et al.*, 1968]. In addition to the rough lava-like flow features apparent in LROC images (Figure 2), secondary cratering of the impact melt and breccia fall-back deposits almost certainly contribute to the high CPR values seen in Figure 1.

[20] The radar-bright parts of the Tycho melt flow have a very disrupted surface structure, but in some cases, larger structural trends are present. The flow drains to the southeast, funneling through terrain gaps. It narrows into a thin, channelized flow (with an overprinted crater) before forming a distinct, oblong pond. Within the pond, the Kaguya Terrain Camera images (Figure 2c) show a series of arcuate ridges perpendicular to the flow direction, and a curving boundary that separates the rougher parts of the flow from

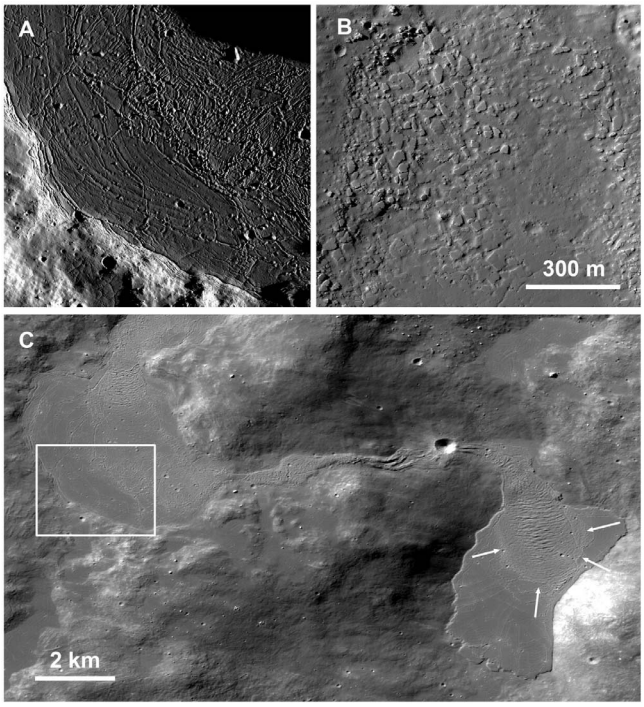

Figure 2. Surface textures associated with different radar backscatter characteristics. (a) High-resolution images from LROC NAC (M116372249) show highly disrupted terrain that corresponds to CPR values greater than one. The roughest areas have ridges, mounds, and upturned plates. (b) An LROC NAC image (M119916367) showing rafted plates. These areas also have elevated CPR values, although the values remain below one. (c) A Kaguya Terrain Camera image showing a section of the southern melt flow and pond. The position of Figure 2a is marked with a white box. The outline of an area of pressure ridges within the pond is marked with arrows. This may represent late stage flow into the pond; alternatively, the pond may have formed via a breakout from an initially smaller flow. Figures 2b and 2c are marked on the radar image in Figure 1.

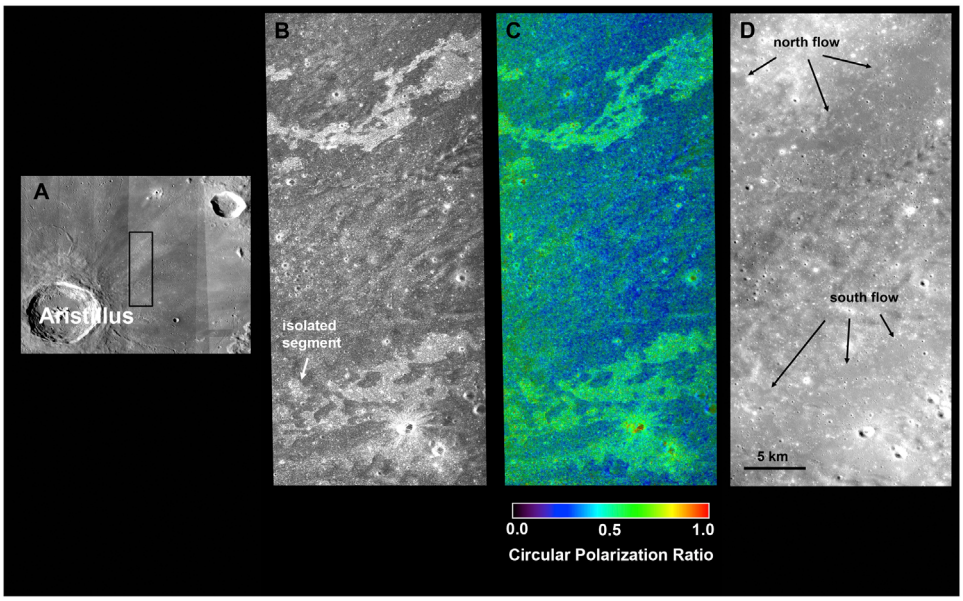

Figure 3. Four images of the impact melt flows northeast of Aristillus. (a) A context image from the LROC WAC mosaic. (b) Mini-RF total power image; radar illumination is from the right. The radar-bright impact melts are mostly connected, but some isolated ponds are present. (c) Mini-RF CPR image, stretched to a color scale and overlaid on the total power image. The impact melts have higher CPR values than the surrounding terrain, but they are less than what is measured for Tycho. The gradient across the image is due to the calibration errors discussed in section 2. (d) Kaguya Terrain Camera image of the same area. The melt flows are barely visible and have been smoothed over by a regolith coating.

smoother ponded material. This ridged area is radar bright with high CPR values. These ridges are similar to pressure ridges seen in terrestrial lava flows, which occur when hot, low-viscosity material moves under a partially cooled, higher viscosity surface [*Fink and Fletcher*, 1978; *Theilig and Greeley*, 1986]. In this case, the flow boundary in the middle of the pond (marked with arrows in Figure 2c) may represent the boundaries of a late-stage melt movement into the pond. Alternately, the smooth parts of the pond may have been created by a breakout of melt from an initial rough flow that subsequently filled in the area to the south.

[21] The surface texture of the pond suggests a complex formation process that may have included multiple influxes of melt that pushed into the pond, and created rough terrain or breakouts, after the flow had partially cooled. Different flow structures are present to the north, where the Mini-RF data show sinuous radar-bright, high-CPR paths that track rougher terrain along the flow direction or at flow terminal areas. These include one area where rafted plates of melt were transported downstream (Figure 2b).

[22] The longest flows observed to date are associated with the 55 km diameter crater Aristillus (33.9°N, 1.2°E) [*Campbell et al.*, 2010]. These flows are long, thin, and extend over 2 crater radii from the rim [*Campbell et al.*, 2010]. In contrast to Tycho, there is little change in backscatter cross-section along the flow and no evidence of channeling. In addition to these long flows, small ponds occur close to the crater rim, and are visible in both optical and radar data. In Mini-RF data, the margins of the long flows have a complex shape that was generated as the melt flowed around multiple topographic obstacles (Figure 3). Most of the radar bright areas are connected, suggesting that the melt was mostly deposited as a topography-constrained flow rather than as individual ponds, although some of the radar bright areas do not have any apparent connection to the main flow. Similar thin melt flows on Venus appear to be caused when melt flows along thin valleys or fractures [*Asimow and Wood*, 1992; *Chadwick and Schaber*, 1993]. The high radar backscatter of the melt deposits suggests that their surface is very rough. The CPR values of the melts are around 0.65 (Figure 3c), which is higher than those of the surrounding terrain, but lower than those of the Tycho melt flows, probably because Aristillus at ~2.1 Ga [*Ryder et al.*, 1991] is significantly older than Tycho (~100 Ma; *Arvidson et al.* [1976]).

[23] The melt flow is barely visible in optical images and looks very similar to surrounding mare basalts. Images acquired with the Kaguya Terrain Camera (10 m/pixel resolution) (Figure 3d) do not show flow features within the radar bright areas, suggesting that the flows are covered by a thin regolith layer. Given the penetration depth of the radar, the surface covering is likely less than a meter. This mantling layer could also explain the lower CPR values, since the radar backscatter would include contributions from both the surface regolith and subsurface rough melt deposit. Because the flow is buried under a greater amount of material than the Tycho melt flow, it is possible that there are smooth parts of the melt flow that are not visible in the radar data; such areas may link some of the distal deposits that appear unconnected in the radar data. Alternatively, some of the unconnected sections of the flow could be ponds that formed when ballistically ejected melt was trapped in depressions.

[24] The fresh crater Jackson (71 km diameter) on the far side of the Moon is similar in size to Tycho and also has a

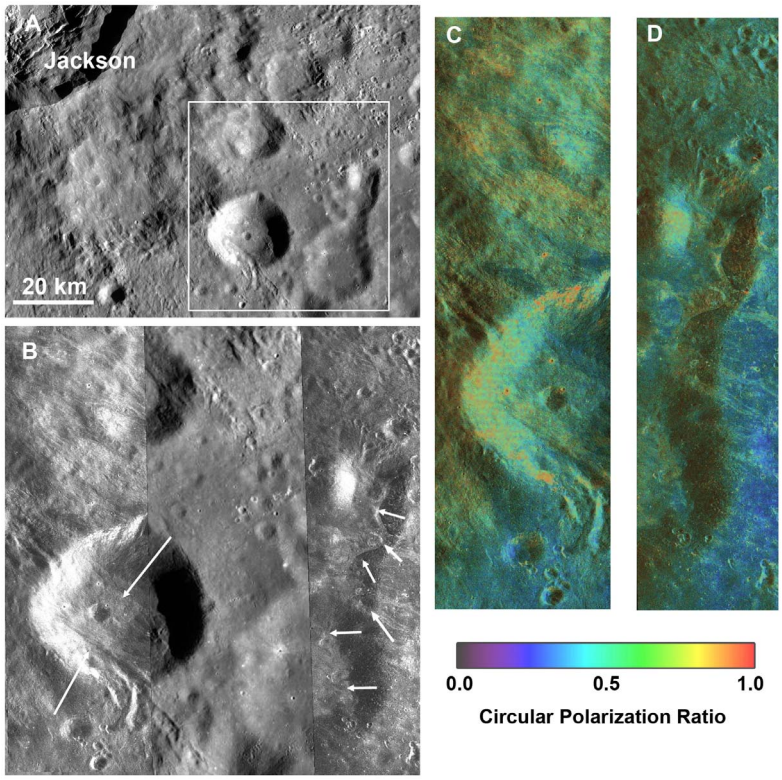

Figure 4. Flow features east of Jackson crater. (a) An LROC WAC context image showing the location of the radar data. (b) Radar total power images (left and right sides) overlaid on the WAC image. Radar illumination is from the right. Arrows mark the positions of flow-like features. Although the features are somewhat brighter than their surroundings, they are not as bright and well-defined as the Tycho and Aristillus melt flows. (c) CPR image of the western radar image in Figure 4b (left) generated by stretching the CPR data to a color scale and overlaying on the total power image. (d) A CPR overlay of the eastern radar image in Figure 4b (right). Parts of the flow features have CPR values that are slightly elevated compared to nearby terrain, but the CPR values are not distinctly different from the proximal ejecta, as is seen at Tycho and Aristillus. Optical images show no evidence of ponded melt. These features may be generated by debris flows.

large ray system. Radar images to the east of the crater show features with a flow-like morphology that are significantly different from the impact melt flows described above. Figure 4a is a LROC Wide-angle Camera (WAC) mosaic image of the area, and Figure 4b shows the Mini-RF total power images on a WAC background with the flow features marked with arrows. The circular polarization ratio images are shown in Figures 4c and 4d. In this case, it looks like material has flowed around and over a series of crater walls (arrows in Figure 4).

[25] The flows have moderate backscatter in the central areas, but are sometimes brighter at the margins and in places where the flows have a contact with an abrupt topographic change (Figure 4b). The lack of radar-bright backscatter from the central regions suggests that the flows are not as rugged as some parts of the melt flows observed at Tycho and Aristillus. The circular polarization ratio values of the flows are higher than surrounding terrain in some areas, but in other places the flows have CPR values that are very similar to the Jackson distal ejecta (Figures 4c and 4d). The flows do not show a distinct high-CPR contrast with their surroundings like the melt flows at Tycho and Aristillus, which suggests that the Jackson flow features may be composed primarily of blocky ejecta. The radar bright flow edges may be caused by rough deposits or by higher topography at the edges of the flow. Since there is no evidence for flowing melted or ponded rock in either radar or optical images, the Jackson flow features may have been caused by debris flows that entrained dust, rock, and small amounts of melt and deposited material at topographic boundaries. These flows may be more similar to some of the debris-rich flows observed in Surveyor 7 images of Tycho than they are to the Tycho melt flows [*Shoemaker et al.*, 1968].

3.2. Medium-Sized Craters (20–50 km Diameter)

[26] Prior imaging analyses have shown that craters in this size range often have significant amounts of melt material that can flow large distances from the source crater [*Hawke and Head*, 1977]. The 43 km diameter crater Glushko (a.k.a. Olbers A; 8°N, 282.4°E) is a good example. Glushko has a complex melt flow pattern similar to that observed at Tycho (Figure 5). LROC Narrow Angle Camera (NAC) images show pressure ridges similar to those seen at Tycho (Figure 5c), but there do not appear to be areas of overturned and rafted plates. Radar-dark areas within the melt flow correspond to cratered ponded areas with fractures. In

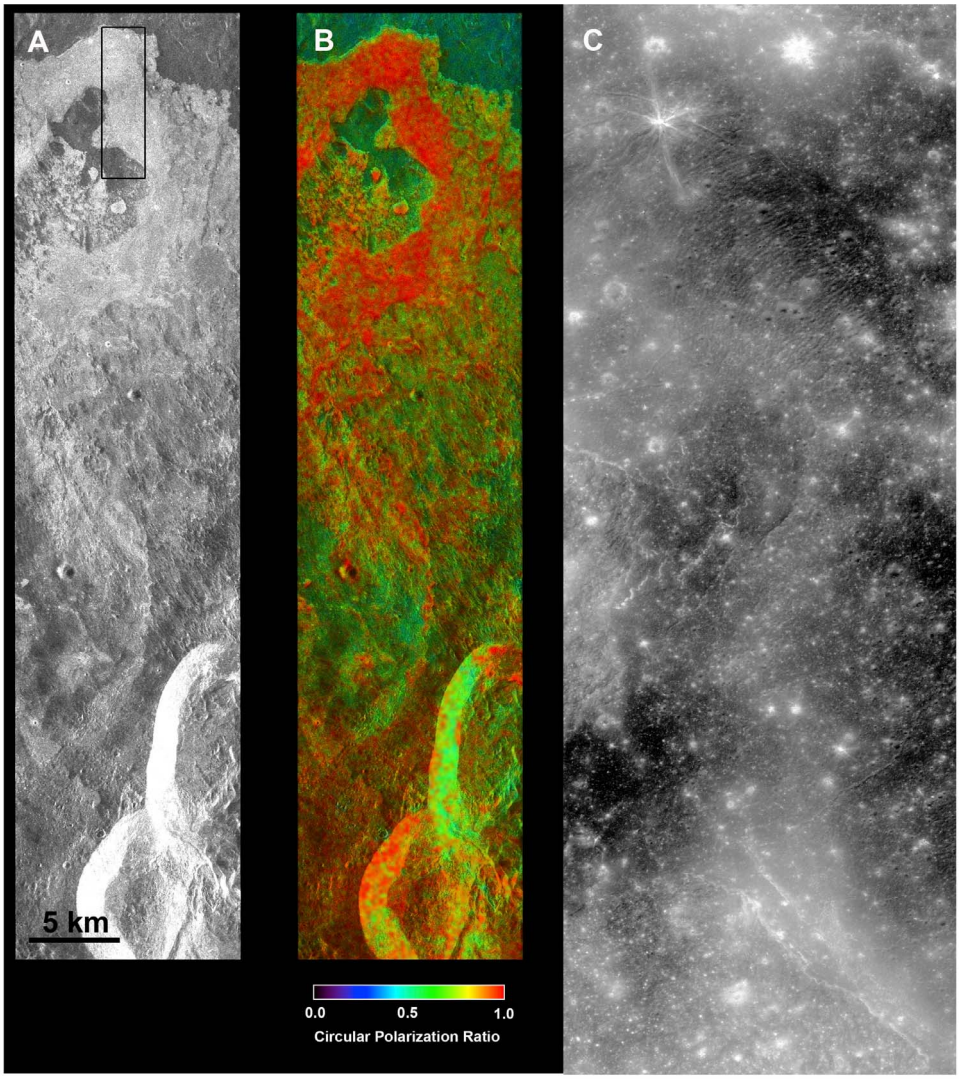

Figure 5. Flows north of the crater Glushko. (a) Mini-RF total power image. Radar illumination is from the right. The location of the image in part C is shown with a box. (b) CPR image stretched to a color scale and overlaid on the total power image. (c) An LROC NAC image of part of the Gluskho flows. As with Tycho, radar-bright, high CPR parts of the flow have rugged flow features, such as pressure ridges. The flow features are not pronounced as they are for Tycho, and the surface may have a thicker mantling layer.

optical images, the surface of the flow is smoother and the flow features are less pronounced than they are for the Tycho flow, suggesting that the surface may be covered by a thicker layer of regolith.

[27] The 26 km diameter crater Gerasimovich D (22.3°S, 238.4°E) also has significant melt deposits, despite not having a radar bright proximal ejecta blanket. A radar-bright impact melt flow extends ~2 crater radii from the rim (Figure 6). The melt flow is barely visible in LROC WAC optical images but has a subdued appearance probably caused by regolith cover (Figure 6a). The flow has a fairly uniform radar brightness compared to the Tycho and Glushko melt flows (Figure 6b), but minor variations are still present. These may be caused by slight differences in the surface texture of the buried flow, or possibly due to smoothing by varying amounts of surface coating. The CPR values are high (0.75), as they are for other radar-bright melt flows.

[28] Another example is the well-known crater Wiener F (47 km diameter; 41.2°N, 150°E), which has both a melt flow and a ponded deposit (Figure 7). Radar images show that the pond is bright with an average CPR value of 0.98. The melt pond surface is rough and ridged, similar to parts of Tycho and Glushko (Figure 7a). A bright flow feature is visible on the pre-existing crater wall that faces toward the impact site. Lunar Orbiter images have a favorable lighting geometry that show a ridge of material corresponding to the radar features. The radar-bright flow on the wall may be either a melt flow that traveled up the wall, a blocky debris flow that was pushed up the wall, or a melt veneer in which the mobile melt drained back into the crater, leaving a lag deposit of unmelted clasts. The rough surface and flow features present on the melt pond surface suggest that the melt

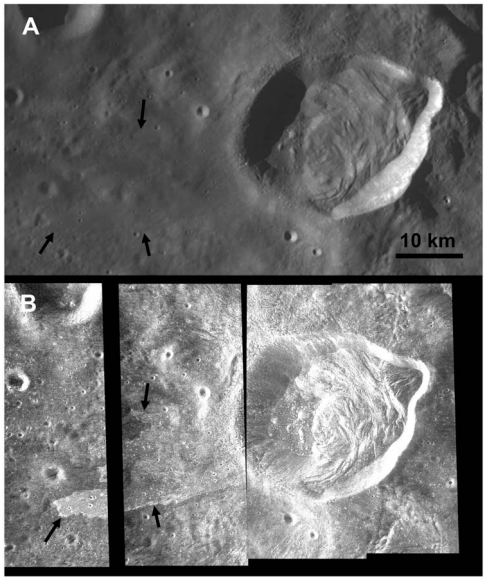

Figure 6. Impact melt flows west of the crater Gerasimovich D. (a) An LROC Wide-Angle Camera image of the crater and surrounding area. The impact melt flows are visible in some places, but are generally covered by regolith. (b) Mini-RF total backscatter power images. Radar illumination is from the left. The radar wave penetrates through thin regolith cover to reveal the flow outlines. The flow has a fairly uniform radar brightness compared to the Tycho and Glushko flows, but there are subtle brightness changes that may indicate smoother and rougher parts of the buried flow or variations in regolith depth.

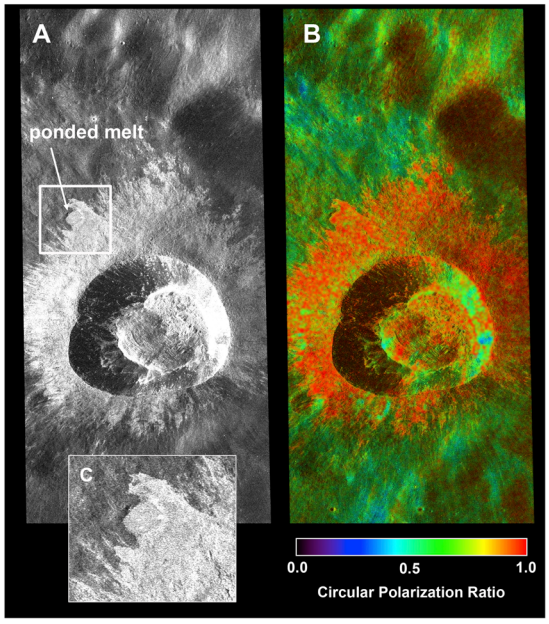

Figure 8. Mini-RF images of a pond associated with a small (13.5 km), unnamed crater (30.9°S, 145.5°E). (a) The total power backscatter radar image. Radar illumination is from the left, and the position of image part C is shown with a box. (b) The circular polarization ratio, stretched to a color scale and overlaid on the total power image. The pond is radar-bright with high CPR values. (c) Total power image of the small pond, which is cratered.

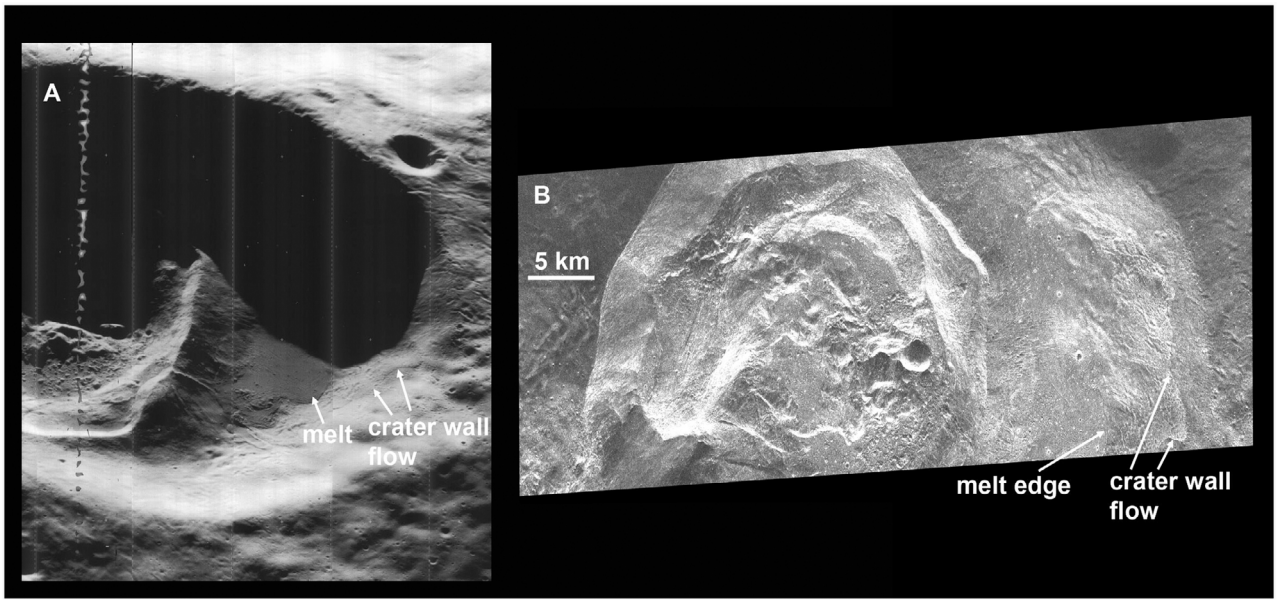

Figure 7. The Wiener F flow and pond. (a) High-resolution Lunar Orbiter images (LO5–103H2 and H3) have a lighting geometry that highlights the structure of the melt pond. The pond has rough ridges on the surface. North is to the right in this image. Arrows highlight the same features in both images: the edge of the melt pond and a flow feature higher on the rim. (b) Mini-RF total power image of the pond. North is to the right, and the radar illumination is from the top. The flow feature on the crater wall is particularly apparent in the radar data.

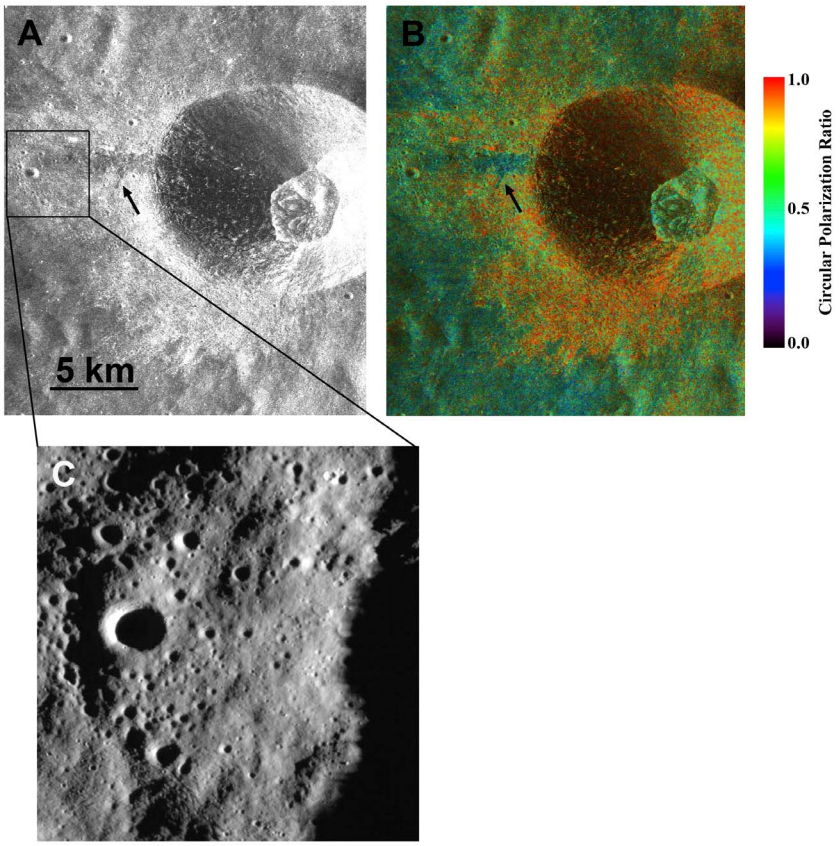

Figure 9. An unnamed 13-km diameter crater (35.7°N, 166.0°E) with an unusual radar-dark lane on top of a possible melt flow or veneer. (a) The radar total power image; illumination is from the left. The location of the Kaguya image in part c is marked with a box. (b) The circular polarization ratio image stretched to a color scale and overlaid on the total power image. (c) A Kaguya image of part of the impact melt and radar-dark region. There is no obvious surface expression of the radar-dark lane. Arrows in Figures 9a and 9b mark the location of a thin outshoot of the dark lane that has rounded edges suggestive of some type of flow.

was not tightly constrained within the topographic boundaries of the preexisting crater, so it was able to flow and develop complex surface features that were frozen in place as it cooled.

3.3. Small Craters (<20 km Diameter)

[29] *Hawke and Head* [1977] observed that large amounts of impact melt first begin to be seen surrounding craters between 10 and 20 km diameter. Mini-RF images of craters within this size range reveal mostly radar bright ponds, veneers, and small flows.

[30] A small, 13.5 km diameter unnamed rayed crater at 30.9°S, 145.5°E (south of Pavlov G) has melt deposits close to its rim. Mini-RF images show a small, radar-bright flow and pond extending ~1 crater radii away from the rim (Figure 8). Like many of the ponds associated with larger craters, the circular polarization values are high and well matched to those of the surrounding ejecta blanket. There are no radar backscatter changes within the melt, suggesting a small amount of melt that cooled quickly.

[31] Another unnamed 13 km diameter crater at (35.7°N, 166.0°E, west of Hutton) appears to have a radar flow or bright ejecta extending from the western edge of the crater rim (Figure 9). The bright melt has an unusual dark lane extending from the rim to the base of the melt. The dark lane has rounded edges and a small offshoot that could indicate that it was caused by some type of flow. Kaguya Terrain Camera imagery (Figure 9c) does not show any obvious explanation for the difference in radar backscatter. The circular polarization ratio image (Figure 9b) shows that the radar-bright ejecta has a high circular polarization ratio, which is consistent with a rough surface of proximal ejecta or melt. The radar-dark lane, however, has a very low CPR, which suggests scattering from terrain that has fewer rocks and more fine material than the surrounding regions. The dark lane may be the result of a landslide or small debris flow from the steep crater rim that left a coating of fine-grained material or removed large blocks. Alternatively, the radar-dark feature may be fine-grained material deposited as part of the impact process.

[32] In another case, possible ejecta flow features are associated with a small, fresh 5 km diameter crater to the northeast of Maunder, in the Orientale basin (Figure 10). In this case, a radar bright deposit appears to have moved downhill to the south and around the topographic contours of Maunder. The radar-bright feature extends ~12 crater radii from the rim. This is a relatively long distance for such a small crater, although there is also a significant downhill

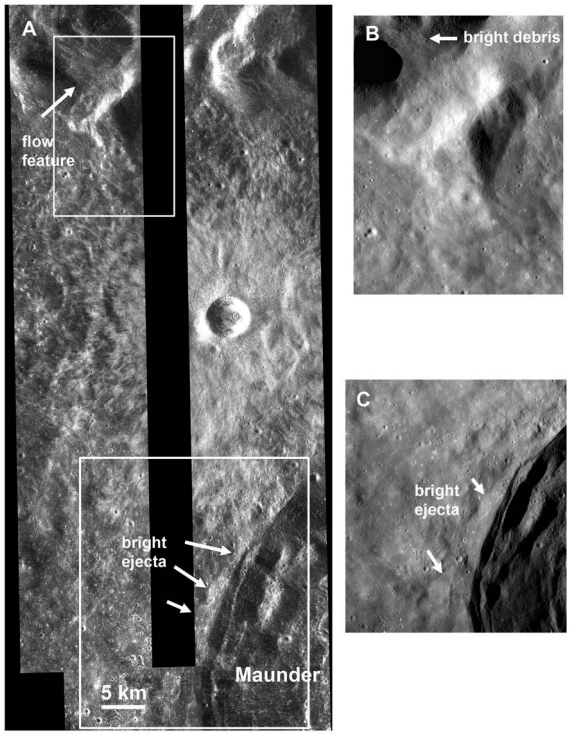

Figure 10. Images of flow features associated with a small (5 km diameter) crater northeast of Maunder crater in the Orientale basin. North is toward the top of the images. (a) A radar total-power image mosaic; illumination is from the left. The location of the images in parts b and c are marked with boxes. Arrows mark the location of flow-like features distant from the central crater. (b) A Kaguya Terrain Camera image of a flow feature northwest of the crater. The feature corresponds to an area of bright debris that appears to have flowed downhill into a valley. (c) A Kaguya Terrain Camera image of radar-bright crater ejecta that has been deposited along the rim of Maunder crater.

slope into Orientale basin in this area. The radar-bright areas do not have flow features (e.g., pressure ridges or channels) associated with them (Figure 10c), and they are optically bright and appear to lie in topographic depressions. Because the distal crater ejecta extends almost as far as the radar-bright feature (10 crater radii in this area), all of the radar-bright areas along the edge of Maunder crater may be rough ejecta from the impact, rather than a melt flow.

[33] To the northwest, there are surface ripples extending out to 6 crater radii, and the bright distal ejecta continue even farther, out to about 9 crater radii. The radar image shows flow features on the side of a low hill that faces away from the impact site (Figure 10a). This feature is darker than most of the crater ejecta in the radar images, and optical images from the Kaguya Terrain Camera show that it is bright, slightly raised terrain (Figure 10b). The CPR values across the flow features are similar to those of the surrounding hills. This may be part of a debris flow from the impact that flowed across the low hills, similar to what is seen at Jackson.

3.4. Melt Deposits With Ambiguous Sources

[34] Two areas appear to have flows and ponds of impact melt that do not have a clear source. One such example is the western side of Keeler crater (11°S, 157°E), where the radar images reveal bright ponds and flows (Figures 11 and 12). Some, but not all, of the melt features are visible in Kaguya Terrain Camera images (Figures 11b and 12). The radar bright ponds have CPR values (~0.7) much higher than the surrounding terrain (~0.3) and similar to those measured for other melt deposits, suggesting that the features are impact melt related and not smooth, block-poor deposits of fine-grained dust. Another similar area at around 41°N and 166°E was identified by *Robinson et al.* [2011] and has similar radar properties, including radar bright ponds and flow features (Figure 13). The ponds are more distinct at this site, and have significantly higher CPR values, possibly because they are less regolith-covered than the Keeler flows and ponds. The high-resolution NAC frames of these features show abundant surface texturing and block fields, consistent with high radar backscatter [*Robinson et al.*, 2011].

[35] Unlike the other flows and ponds discussed in prior sections, these features are not clearly associated with the rim or ejecta blanket of a specific crater. Instead, melt appears to have flowed downhill into many topographic lows covering a broad area. One possible explanation is that the melts were produced by oblique impacts that deposit a significant amount of melted material downrange, or to the sides of, the impact site. Similar features exist on Venus; for example, at Graham crater (1°N, 6°E), where some material is trapped in small ponds on a hill [*Schultz*, 1992]. However, oblique impacts on the smooth Venus plains also generate significant flow features, in part because of the higher temperatures and higher mean impact velocities that produce a larger amount of melt, and in part because the terrain is often not rugged enough to trap the melt in many small ponds.

[36] Identifying a source crater for the extensive melt deposits is difficult in the heavily cratered highlands. For example, the Keeler site has a young impact crater (Ventris M) to the north with a ray system that is noticeably symmetric, although the crater rim is slightly elliptical. However, the crater is ~120 km distant, and there is no evidence for extensive melt deposits near the crater itself. Another nearby oblique impact crater is Keeler V, but in this case, some of the impact melt clearly flows over the rim and into the Keeler V floor (Figure 11d), which suggests a different source. Keeler V is also older and more degraded than other nearby craters, so it is unlikely to have retained clear melt deposits. The source crater may also have been a nearby, less oblique impact that did not produce a crater rim that deviates from circular. The 37 km diameter crater Plante′, inside Keeler crater, has impact melt flows extending from the proximal ejecta blanket, but is also over 100 km distant. The crater Keeler S is the closest crater to the site. It does not have a radar bright ejecta blanket or evidence of near-rim melt deposits, but neither does Gerasimovich D, which has a large melt flow. Regardless of the source, these isolated melt deposits are interesting in that they suggest that impact melts may cover substantial areas even in heavily cratered terrains and may remain visible even as the source crater proximal ejecta ages and weathers to blend into the surrounding terrain.

4. Discussion

[37] The radar data described above can be used to assess the surface roughness of the lunar impact melts compared to

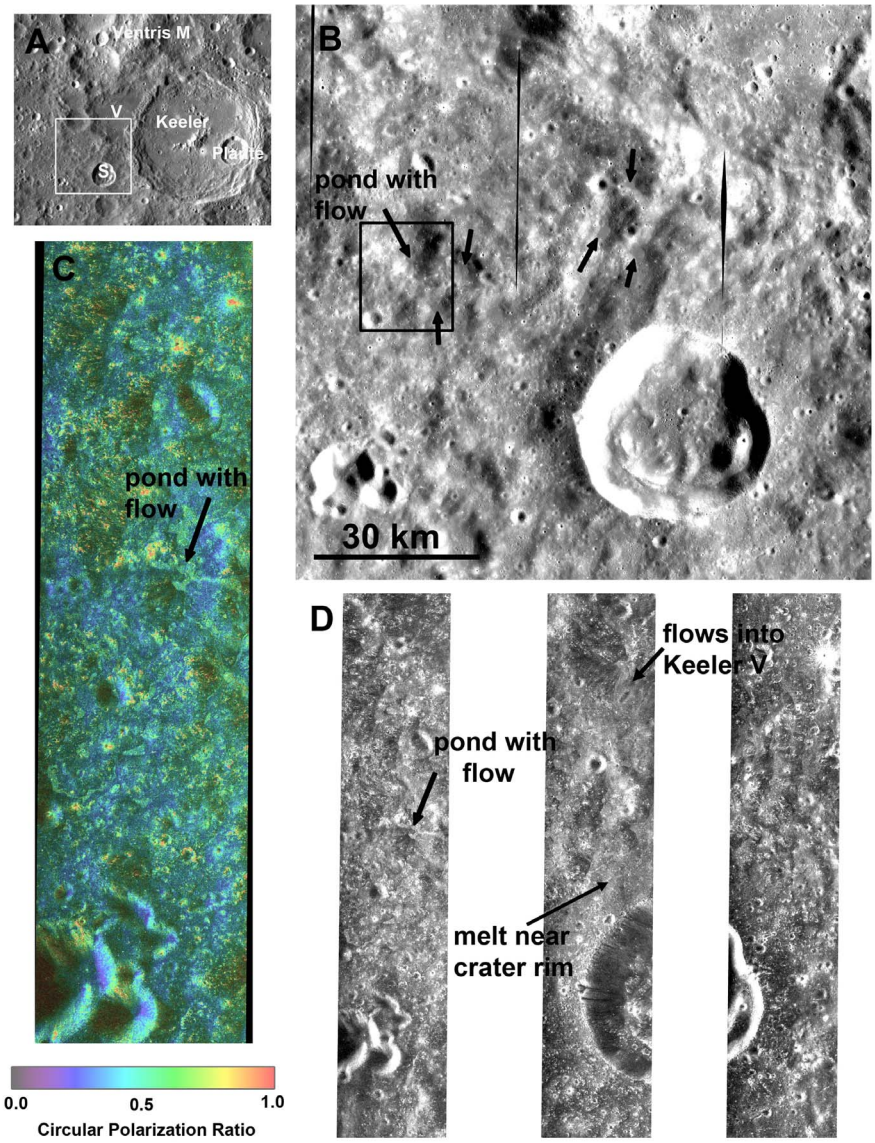

Figure 11. Images of ponds and flows near Keeler crater. Most of the melt is north of the crater Keeler S. (a) A LROC WAC context image with craters labeled. A box marks the locations of parts b and d. (b) A Kaguya Terrain Camera image of the area of ponds. Some of the more easily visible ponds are marked with arrows. An arrow also marks the location of a small pond and flow that is easily visible in the radar data. A box marks the area covered by the close-up images in Figure 12. (c) A circular polarization ratio image of part of the melt pond field. This image corresponds to the left-most radar image in part d. The location of the small pond and flow is marked. Most of the ponds have CPR values between 0.6 and 0.7, suggesting that they are rougher than their surroundings, but probably partially buried. (d) Radar total backscatter images of the area shown in part b. The backscatter images show multiple radar-bright ponds and flow features, including flows into Keeler V. Radar illumination is from the left.

terrestrial lava flows. Many of the melt flows have a very uniform, radar bright appearance, as reported by *Campbell et al.* [2010]. However, in some cases, the flow changes both in backscatter and circular polarization ratio along the flow. Terrestrial a'a flows have CPRs between 0.3 and 0.6 at incidence angles of 40–50 [*Campbell and Campbell*, 1992]. Blocky lava flows like SP Flow (north of Flagstaff, Arizona) have CPRs of 0.8–1.2 at the same incidence angles, at 24 cm wavelength [*Campbell and Campbell*, 1992]. At shorter wavelengths, the flows have somewhat higher CPR values. The CPR values of the radar bright lunar melt flows are often greater than those of terrestrial a'a flows and similar to those of blocky lava flows like SP Flow, which suggests that the flows have extremely rugged surfaces at centimeter to meter scales. In cases where the CPR values of the bright flows are somewhat lower in some of the older craters (e.g.,

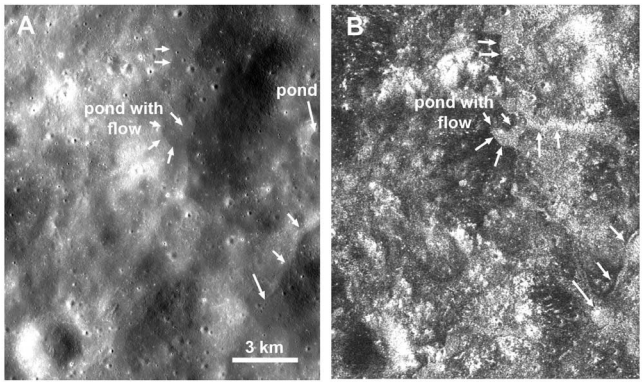

Figure 12. A close-up view of Keeler-area melt ponds and flows. The image location is marked in Figure 11. (a) Kaguya image with ponds marked. (b) Corresponding total power radar image. Note that in the optical image, the illumination is from the right but in the radar image, the illumination is from the left. Arrows mark the position of ponded material at the bottom of a hill. The radar image shows a radar bright streak that could be melt material that flowed down the side of the hill. On the right side of the optical image, there is a pond that does not appear to show up in the radar data, probably because the radar viewing geometry shifts the bottom of the crater off the edge of the image. An additional, barely visible, pond is visible in the lower right of the image. Arrows mark the pond and a slightly flat sinuous ridge leading down to the pond.

Aristillus, Gerasimovich D) the melt flows appear partially buried in optical images, which likely reduces the CPR. Ponded deposits that appear smooth in optical data still have CPR values as great as terrestrial a'a flows [*Campbell and Campbell*, 1992], probably due to a combination of initial rough surface texture subsequently filled in by dust, fallback breccia deposited on the surface, the presence of small impact craters and related blocky ejecta, surface cooling fractures, and embedded county rock clasts.

[38] So far, within the resolution limit of the Mini-RF radar, there are no examples of small craters (<20 km) with complex flows showing significant backscatter and circular polarization ratio variations along the flow. The impact melt deposits of small craters are always radar-bright with high CPR values. The surfaces of many of the small flows and ponds may have cooled fairly quickly, before they had time to form smooth surfaces. In the case of larger craters, like Tycho and Glushko, late stage injection of melt from draining ponds at higher elevations may have broken up a previously frozen surface and created a very rugged and broken terrain.

[39] In some cases, particularly for rough radar-bright flows, the radar data often provides a more useful view of flow margins than optical data, where the surface can be mantled by fine-grained regolith. Young impact craters, such as Tycho, have relatively unburied melts that are readily apparent in both radar and optical data. Many of the melt deposits and flows described here are associated with craters that have ray systems and hence are geologically young. Over time, the crater ejecta, including ray systems and ejecta flows, are destroyed and buried by subsequent impacts.

[40] *Ghent et al.* [2005] showed that younger craters often have radar-dark haloes in 70-cm wavelength radar data, and that older craters do not have these haloes. These haloes have been attributed to a layer of fine-grained ejecta mantling that becomes mixed into the underlying, blocky ejecta blanket over time [*Ghent et al.*, 2005]. Two of the features with impact melts have radar dark haloes (Tycho and Aristillus), but the others discussed above are located on the lunar limb or farside where no 70-cm wavelength radar data is currently available. There is clearly a process by which ray systems, radar dark haloes, and ejecta flow features are erased, but it is not yet clear what timeline this process follows or how it varies with crater size. Future comprehensive searches of the radar data will help to improve the statistics of which types and ages of craters have melt deposits and ejecta flows.

[41] The combination of radar and optical data for the lunar impact melts also has some implications for the surface textures of impact melt flows on Venus, for which only radar data is available. In particular, as proposed by *Johnson and Baker* [1994], the lunar data suggest that many of the changes in radar reflectivity within large complex melt flows are probably due to flow features similar to those seen in terrestrial lava flows, such as ponding, rafted and overturned plates, channeling, and pressure ridges. Some of the Venus flows appear darker to the radar and have been interpreted as turbulent run-out flows that carry debris [*Schultz*, 1992]. These Venus flows have some similar radar characteristics to the flows associated with Jackson and the small crater near Maunder, which are darker to the radar and show no optical evidence for flowing, melted rock. The impact process may

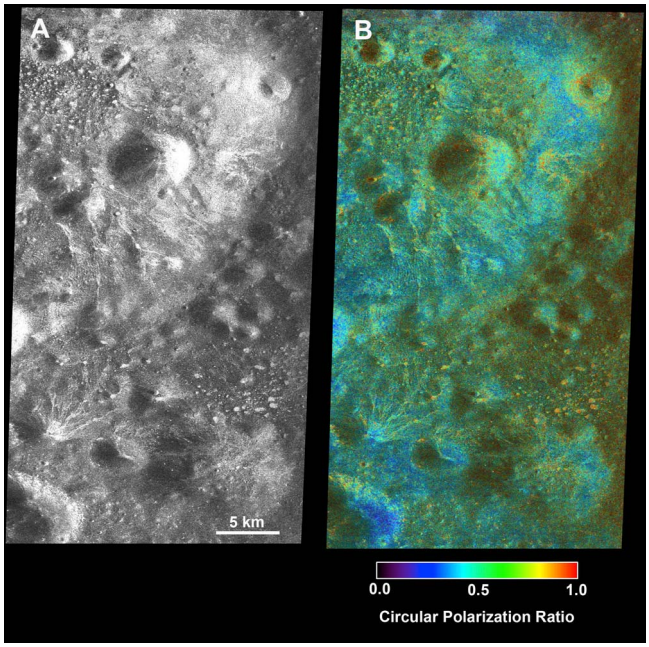

Figure 13. Mini-RF images of the pond field located at 41°N and 166°E [*Robinson et al.*, 2011]. (a) Total backscatter power. (b) Circular polarization ratio image stretched to a color scale and overlaid on the total power image. The ponds at this site have higher CPR values than the ponds at Keeler, but they also appear to be less buried in both radar and optical imagery [*Robinson et al.*, 2011]. Radar illumination is from the left.

sometimes produce debris flows that are visible in radar images due to the sharp contrast in topography and roughness of the emplaced material relative to the surroundings.

5. Summary and Future Work

[42] Recent radar imaging data suggests that impact melt flows and ponds are more common on the Moon than was previously known. The CPR values of the melt flows are generally high and most of the flows have very rugged surfaces. Some lunar impacts cause debris to be deposited in a flow-like manner, and these flows are often visible in radar images due to their rough edges and topographic expression. Future work will aim to achieve better statistics on the number and size of craters with melt flows and ponds. The Mini-RF data will be useful for understanding the amount of melt produced by impacts, as well as the directions in which most of the melt traveled. A systematic search of young and rayed crater systems using high resolution radar imaging is likely to yield additional data on buried and partially buried melt flows, including how the melt flows are buried and eroded over time.

[43] **Acknowledgments.** We thank the Mini-RF engineering and operations teams for their work in building the instrument and acquiring the data. We also thank the LRO LROC and Kaguya (SELENE) Terrain Camera teams for their efforts to provide the publicly available data sets used in this work. Thanks to Veronica Bray and Wenzhe Fa who provided detailed and helpful reviews. This project was supported through a NASA LRO Participating Scientist grant (NNX08AM80G) to L. Carter.

References

Arvidson, R., R. Drozd, E. Guiness, C. Hohenberg, C. Morgan, R. Morrison, and V. Oberbeck (1976), Cosmic ray exposure age of Apollo 17 samples and the age of Tycho, *Proc. Lunar Sci. Conf.*, *7*, 2817–2832.

Asimow, P. D., and J. A. Wood (1992), Fluid outflows from Venus impact craters: Analysis from Magellan data, *J. Geophys. Res.*, *97*(E8), 13,643–13,665, doi:10.1029/92JE00981.

Bray, V. J., et al. (2010), New insight into lunar impact melt mobility from the LRO camera, *Geophys. Res. Lett.*, *37*, L21202, doi:10.1029/2010GL044666.

Campbell, B. A. (2009), Scale dependent surface roughness behavior and its impact on empirical models for radar backscatter, *IEEE Trans. Geosci. Remote Sens.*, *47*, 3480–3488, doi:10.1109/TGRS.2009.2022752.

Campbell, B. A., and D. B. Campbell (1992), Analysis of volcanic surface morphology on Venus from comparison of Arecibo, Magellan, and terrestrial airborne radar data, *J. Geophys. Res.*, *97*(E10), 16,293–16,314, doi:10.1029/92JE01558.

Campbell, B. A., L. M. Carter, D. B. Campbell, M. C. Nolan, J. F. Chandler, R. R. Ghent, B. R. Hawke, R. F. Anderson, and K. S. Wells (2010), Earth-Based S-band radar mapping of the Moon: New views of impact melt distribution and mare physical properties, *Icarus*, *208*, doi:10.1016/j.icarus.2010.03.011.

Carrier, W. D., G. R. Ohloeft, and W. Mendell (1991), Physical properties of the lunar surface, in *Lunar Sourcebook*, edited by G. Heiken, D. Vaniman, and B. M. French, pp. 475–567, Cambridge Univ. Press, New York.

Carter, L. M., B. A. Campbell, B. R. Hawke, D. B. Campbell, and M. C. Nolan (2009), Radar remote sensing of pyroclastic deposits in the Mare Serenitatis and Mare Vaporum regions of the Moon, *J. Geophys. Res.*, *114*, E11004, doi:10.1029/2009JE003406.

Carter, L. M., D. B. Campbell, and B. A. Campbell (2011), Geologic studies of planetary surfaces using radar polarimetric imaging, *Proc. IEEE*, *99*, doi:10.1109/JPROC.2010.2099090.

Chadwick, D. J., and G. G. Schaber (1993), Impact crater outflows on Venus: Morphology and emplacement mechanisms, *J. Geophys. Res.*, *98*(E11), 20,891–20,902, doi:10.1029/93JE02605.

Fink, J. H., and R. C. Fletcher (1978), Ropy Pahoehoe: Surface folding of a viscous fluid, *J. Volcanol. Geotherm. Res.*, *4*, 151–170, doi:10.1016/0377-0273(78)90034-3.

Ghent, R. R., D. W. Leverington, B. A. Campbell, B. R. Hawke, and D. B. Campbell (2005), Earth-based observations of radar-dark crater haloes on the Moon: Implications for regolith properties, *J. Geophys. Res.*, *110*, E02005, doi:10.1029/2004JE002366.

Green, P. E. (1968), Radar measurements of target scattering properties, in *Radar Astronomy*, edited by J. V. Evans and T. Hagfors, pp. 1–77, McGraw-Hill, New York.

Guest, J. E. (1973), Stratigraphy of ejecta from the lunar crater Aristarchus, *Geol. Soc. Am. Bull.*, *84*, 2873–2894, doi:10.1130/0016-7606(1973)84<2873:SOEFTL>2.0.CO;2.

Hawke, B. R., and J. W. Head (1977), Impact melt on lunar crater rims, in *Impact and Explosion Cratering*, edited by D. J. Roddy, R. O. Pepin, and R. B. Merrill, pp. 815–841, Pergamon Press, New York.

Howard, K. A., and H. G. Wilshire (1975), Flows of impact melt at lunar craters, *J. Res. U.S. Geol. Surv.*, *3*(2), 237–251.

Jackson, J. D. (1999), *Classical Electrodynamics*, 3rd ed., John Wiley, New York.

Johnson, J. R., and V. R. Baker (1994), Surface property variations in Venusian fluidized ejecta blanket craters, *Icarus*, *110*, 33–70, doi:10.1006/icar.1994.1106.

Phillips, R. J., R. E. Arvidson, J. M. Boyce, D. B. Campbell, J. E. Guest, G. G. Schaber, and L. A. Soderblom (1991), Impact craters on Venus: Initial analysis from Magellan, *Science*, *252*, 288–297, doi:10.1126/science.252.5003.288.

Pierazzo, E., and H. J. Melosh (2000), Melt production in oblique impacts, *Icarus*, *145*, 252–261, doi:10.1006/icar.1999.6332.

Raney, R. K., et al. (2011), The Lunar Mini-RF radars: Hybrid polarimetric architecture and initial results, *Proc. IEEE*, *99*, 808–823, doi:10.1109/JPROC.2010.2084970.

Robinson, M. S., et al. (2010), Lunar Reconnaissance Orbiter Camera (LROC) instrument overview, *Space Sci. Rev.*, *150*, 81–124, doi:10.1007/s11214-010-9634–2.

Robinson, M. S., P. C. Thomas, B. W. Denevi, T. Tran, E. B. Cisneros, J. Plescia, C. H. van der Bogert, and H. Hiesinger (2011), Highland smooth plains, an exceptional grouping, *Lunar Plan. Sci. Conf.*, *42nd*, Abstract 2511.

Ryder, G., D. Bogard, and D. Garrison (1991), Probable age of Autolycus and calibration of lunar stratigraphy, *Geology*, *19*, 143–146, doi:10.1130/0091-7613(1991)019<0143:PAOAAC>2.3.CO;2.

Schultz, P. H. (1992), Atmospheric effects on ejecta emplacement and crater formation on Venus from Magellan, *J. Geophys. Res.*, *97*(E10), 16,183–16,248, doi:10.1029/92JE01508.

Schultz, P. H. (1996), Effect of impact angle on vaporization, *J. Geophys. Res.*, *101*(E9), 21,117–21,136, doi:10.1029/96JE02266.

Shoemaker, E. M., R. M. Batson, H. E. Hole, E. C. Morris, J. J. Rennilson, and E. A. Whitaker (1968), Television observations from Surveyor VII, *NASA Spec. Publ.*, *SP-173*, 13–81.

Stacy, N. J. S. (1993), High resolution synthetic aperture radar observations of the Moon, Ph.D. diss., Dept. of Astron., Cornell Univ., Ithaca, New York.

Theilig, E., and R. Greeley (1986), Lava flows on Mars: Analysis of small surface features and comparisons with terrestrial analogs, *J. Geophys. Res.*, *91*(B13), E193–E206, doi:10.1029/JB091iB13p0E193.

Ulaby, F. T., R. K. Moore, and A. K. Fung (1986), *Microwave Remote Sensing: Active and Passive*, vol. II, *Radar Remote Sensing and Surface Scattering and Emission Theory*, 608 pp., Artech House, Norwood, Mass.

D. B. J. Bussey, J. T. Cahill, C. D. Neish, G. W. Patterson, and R. K. Raney, Johns Hopkins University Applied Physics Laboratory, 11100 Johns Hopkins Rd., Laurel, MD 20723, USA.

L. M. Carter, Planetary Geodynamics Laboratory, NASA Goddard Space Flight Center, Code 698, Greenbelt, MD 20771, USA. (lynn.m.carter@nasa.gov)

P. D. Spudis, Lunar and Planetary Institute, 3600 Bay Area Blvd., Houston, TX 77058, USA.